Eur. Phys. J. B **36**, 271–279 (2003)
DOI: 10.1140/epjb/e2003-00344-7

THE EUROPEAN PHYSICAL JOURNAL B

Characterization of anti-phase boundaries in epitaxial magnetite films

S. Celotto[1], W. Eerenstein[2,a], and T. Hibma[2]

[1] Department of Engineering, Materials Science and Engineering, University of Liverpool, Brownlow Hill, Liverpool L69 3BX, UK
[2] Materials Science Centre, University of Groningen, Nijenborgh 4, 9747 AG, Groningen, The Netherlands

Received 22 May 2003
Published online 8 December 2003 –

Abstract. The occurrence of anti-phase domain boundaries (APBs) in epitaxial Fe_3O_4 films has a strong influence on the resistivity, magnetic and magneto-resistance properties of these films. It is therefore important to understand the configuration and magnetic coupling across the boundary. We have studied the distribution of shift vectors and the relationship between the shift vector and the boundary plane and the resulting magnetic coupling at the boundary. The vast majority of APBs have $1/4\langle 110\rangle$ shifts while those with 1/2[100] shift are very uncommon. Approximately 45% of APBs have shift vectors in the plane of the film. Their boundary plane is perpendicular to the shift vectors and in this case the magnetic coupling can be either ferromagnetic or anti-ferromagnetic. The remaining 55% of APBs have shift vectors out of the film plane, with the boundary planes not perpendicular to the shift vector but close to {100} or {310}, resulting in a ferromagnetic coupling when the boundary plane is {100} and in an anti-ferromagnetic coupling when the boundary plane is {310}.

PACS. 68.37.Lp Transmission electron microscopy (TEM) (including STEM, HRTEM, etc.) – 75.30.Et Exchange and superexchange interactions – 75.70.Cn Magnetic properties of interfaces (multilayers, superlattices, heterostructures)

1 Introduction

Epitaxial Fe_3O_4 ultra-thin films have physical properties that differ significantly from those of the bulk. They exhibit magneto-resistance [1–3], larger electrical resistivity [4,5] and the magnetisation does not saturate in high fields [6]. These properties are a consequence of the high density of anti-phase boundaries (APBs) present in epitaxially grown thin films. At the APBs a strong anti-ferromagnetic coupling can be present [6,7], which influences the magnetic, conducting and magneto-resistance properties of the epitaxial films. It is therefore important to have knowledge about the APB character, the relationship between the shift and the boundary plane, and the way it influences the magnetic coupling across the APB.

Fe_3O_4 grows epitaxially on MgO in a layer-by-layer growth mode, where one layer consists of 1/4 of the Fe_3O_4 unit cell [8]. APBs form when islands of Fe_3O_4 on the MgO surface coalesce and the neighboring islands are shifted with respect to each other [9]. The APB shifts in these films are a consequence of two distinct forms of symmetry breaking between MgO and Fe_3O_4. The first is due to the lattice parameter of MgO (0.4212 nm) being half that of Fe_3O_4 (0.8397 nm) and thus two adjacent Fe_3O_4 monolayers may be shifted by 1/4[110], $1/4[1\bar{1}0]$ or by 1/2[100] as shown in Figure 1. The other APB shifts are a result of the lower symmetry of Fe_3O_4 monolayers compared to the MgO substrate surface, where the former is 2m and the latter is 4m. Consequently, adjacent Fe_3O_4 islands on the same MgO surface may be rotated by 90°, also shown schematically in Figure 1. In combination with the screw symmetry element of the spinel structure this gives rise to the $1/4[101]$, $1/4[10\bar{1}]$, 1/4[011] and $1/4[01\bar{1}]$ shifts. Growth from regions on the MgO substrate separated by a stepheight of half a unit cell of MgO (0.2106 nm) can also give rise to these shifts. In this study we designate the 1/4[110], $1/4[1\bar{1}0]$ and the 1/2[100] shifts to be the in-plane shifts (i.e plane of the film) and the $1/4[101]$, $1/4[10\bar{1}]$, 1/4[011] and $1/4[01\bar{1}]$ shifts to be the out-of-plane shifts. Note that the oxygen sublattice is more or less undisturbed across the APBs and only the cation lattice is shifted.

It has been reported that the domain size in Fe_3O_4 films grown by MBE is largely dependent on the film thickness, growth temperature, post-annealing time and oxygen

[a] *Present address*: Dept. of Materials Science, University of Cambridge, Pembroke Street, Cambridge CB2 3QZ, UK
e-mail: we212@cam.ac.uk

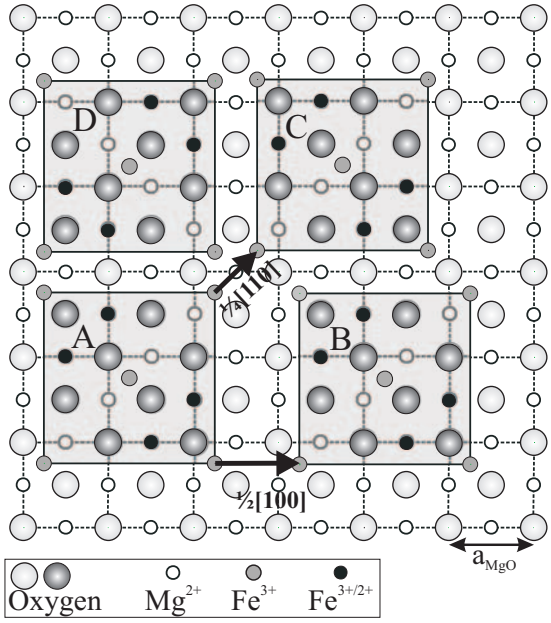

Fig. 1. Schematic illustration showing APB shifts can be formed based on the different translation and rotation symmetry respectively of the first Fe_3O_4 monolayer and the MgO surface. Represented on the MgO surface are unit cells of Fe_3O_4 monolayers shifted relative to the reference (A) to form the in-plane shifts of (B) 1/2[100] and (C) 1/4[110], and a rotated monolayer (D) that can form an out-of-plane shift.

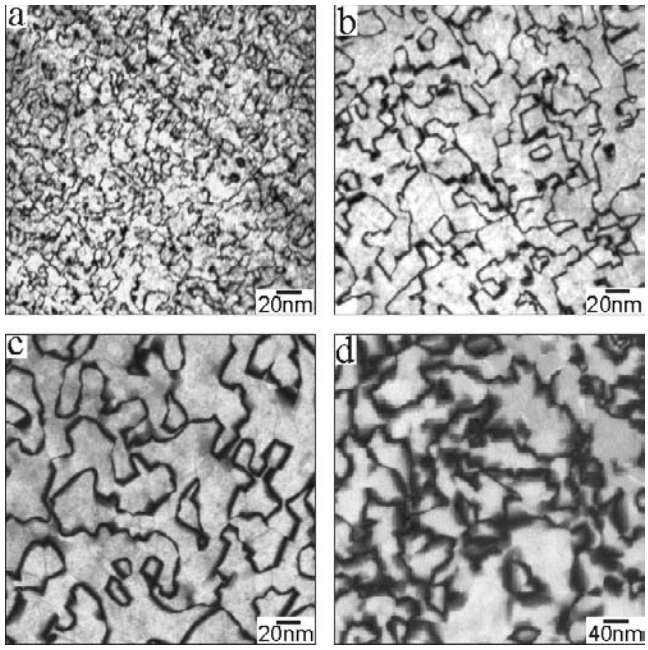

Fig. 2. TEM dark field images of (a) 6 nm, (b) 12 nm (c) 25 nm and (d) 50 nm thick Fe_3O_4 films on cleaved MgO grown at 250 °C. Images were taken near the [001] direction using the 220 type reflection.

flux [10]. The domain size increases with film thickness and with increasing growth or annealing temperature. Analysis of coarsening rates during annealing after growth at various temperatures show that the APBs migrate via a thermally activated diffusional process.

In this article we present a study of the APB shift in Fe_3O_4 films, the directionality of the APBs, and the relationship between APB shift vectors with the average boundary plane. The consequences for the magnetic exchange coupling across the APB will also be discussed.

2 Experimental

The Fe_3O_4 films were grown using molecular beam epitaxy (MBE) in an ultra-high vacuum system with a background pressure of 10^{-10} mbar. Standard samples were grown using an iron flux of 1.2 Å/min, an oxygen pressure of 10^{-6} mbar and a growth temperature of 250 °C. Using these conditions, films of 6, 12, 25 and 50 nm thickness have been grown. To determine the structural quality and purity, the films were analysed in situ using RHEED, LEED and XPS. No contaminations were detected with XPS. The structural quality as determined from RHEED and LEED was very good, with Kikuchi lines still visible in the RHEED patterns and both RHEED and LEED images having a very low background intensity. The lattice constant was determined from XRD, resulting in an c-axis value of 8.34 Å (the c-axis is slightly compressed with respect to the bulk due the the in-plane expansion resulting from the epitaxial growth on MgO). The thickness of the films was determined during growth from the oscillation period of the RHEED specular spot intensity. Because of the layer-by-layer growth mode, the film thickness can be determined very accurately from the RHEED intensity oscillations [8]. The iron flux was measured using a quartz crystal balance. Oxygen was admitted via a gas delivery system that consists of a small buffer volume. The O_2-gas is let into the buffer volume via a leak valve. The buffer pressure is measured with a baratron. The stoichiometry of the films was determined using Mössbauer spectroscopy. All films were highly stoichiometric, the deviation from stoichiometry as expressed by writing the composition as $Fe_{3-\delta}O_4$ was as low as $\delta < 0.008$.

The APB morphology was studied by transmission electron microscopy (TEM). Specimens were prepared by dissolving the MgO substrate and floating the Fe_3O_4 films off in a 4 wt.% ammonium sulphate solution at 70 °C. The Fe_3O_4 films were picked up on a copper grid and analysed in a JEOL 2000FX transmission electron microscope operating at 200 keV.

3 Results

3.1 APB morphology

The APB morphologies of four Fe_3O_4 films of different thickness from 6 to 50 nm are shown in Figure 2. The figure shows an increase in domain size with increasing thickness. The increase in domain size can also clearly be seen in post annealed samples as shown in Figure 3 for

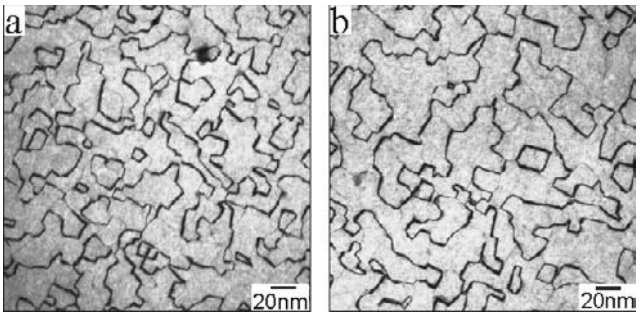

Fig. 3. TEM dark field images of 12 nm thick films grown at 250 °C and post annealed at 300 °C for: (a) 2 hours and (b) 10 hours. Images were taken near the [001] direction using the 220-type reflection.

a 12 nm thick film post annealed at 300 °C for 2 and 4 hours. Figures 2 and 3 show four principle changes with increasing thickness and annealing time: i) an increase in domain size, ii) a decrease in curvature, iii) an increase in directionality, and iv) a decrease in the number of boundary intersections and boundaries per intersection. The latter three are less obvious in the thicker films (> 25 nm) because of the larger projected width of the APBs. The above trends in the APB morphologies were also observed with increasing growth temperature and annealing temperature [10]. The increase in domain size and the decrease in the number of boundary junctions is a consequence of the APBs annealing out of the films with time at temperature during growth and similarly with annealing time. Note that in these ultra-thin films stacking-fault-like fringes in APBs are absent because the thickness is significantly less than an extinction distance of Fe_3O_4 (213 nm for the 220-reflection).

In the following, we will first present results of the directionality of the APBs as a function of film thickness and annealing and the relationship to the crystallographic planes in the Fe_3O_4 lattice. Then we present the analysis of the APB shifts and their relationship to the approximate boundary planes.

3.2 Directionality and inclination of APBs

The directionality of the APBs was studied using image analysis on dark field images taken close to the [001] zone axis using the 220-type reflection. Figure 4 shows the degree of directionality using rose diagrams for 12 nm thick films post annealed at 300 °C.

The directionality of the APBs is predominantly close to $\pm[100]$ and $\pm[010]$ and increases with annealing time. It can be seen from Figure 4c and particularly in Figure 4d that the directionality also develops a bias in the direction either side of these $\langle 100 \rangle$, indicated in the figure by dashed lines. The average angle between the lobes and the $\langle 100 \rangle$ are approximately 18° once the angular deviation and asymmetry due to tilting away from the exact [001] zone axis is taken into account. These lobes lie close to the $\langle 130 \rangle$, which lie at 18.4° either side of the $\langle 100 \rangle$.

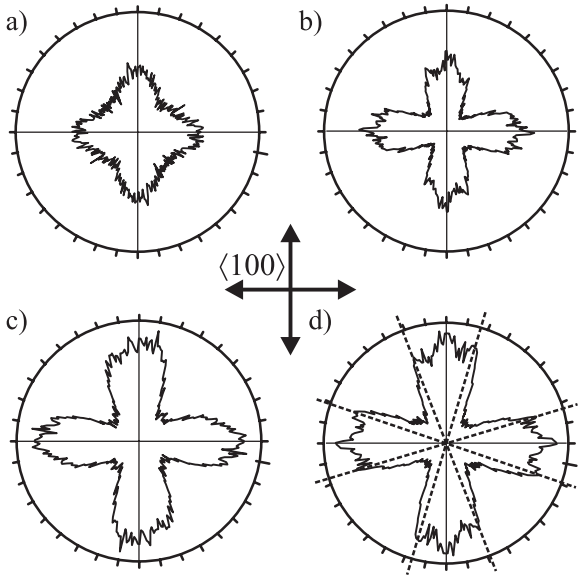

Fig. 4. Rose diagrams showing the directionality of the APB projections in 12 nm thick films (grown at 250 °C): (a) initial, (b) 1 hour, (c) 2hrs, and (d) 10 hrs post annealing at 250 °C. The projection directions are near the [001], but the tilt from the zone axis to obtain a two-beam diffraction condition produces asymmetry in some of the rose diagrams. The $\langle 100 \rangle$ directions are indicated by the thick arrows. The dashed lines in d) indicate the $\langle 310 \rangle$ directions.

Similar results, though more accelerated, were observed at higher post-annealing temperatures.

The increased directionality was also observed with increasing thickness as shown in Figure 2, but is less obvious in the thicker films (> 25 nm) because of the relatively large projected width of the APBs.

The inclination of the boundaries through the films can be determined using the projected width measured near the [001], in conjunction with the thickness of the films. In all of the films the inclination varied from 2° to 13° with a fairly consistent average of 7.5°. No significant relationship between the projected width and direction was observed.

3.3 Shift vector of the anti-phase boundary

The visibility criteria for APBs are equivalent to those of stacking faults, i.e. they are visible when the phase change $\alpha = 2\pi \mathbf{g} \cdot \mathbf{R} = (2N + 1)\pi$ and otherwise invisible, where $\mathbf{g}$ is the operating reflection, $\mathbf{R}$ is the shift vector of the APB and N is an integer. The specific shifts can be determined with a series of systematic dark-field images taken close to a two-beam condition, and identifying whether the APB is visible or invisible. The relationship between APB visibility and the diffracting vectors used here are shown in Table 1. In the images shown in Figures 2 and 3, only the APBs with out-of-plane shifts are visible. APBs with in-plane shifts become visible by tilting to other zone axes and using different diffracting vectors.

Table 1. The visibility criteria used to identify the APB shifts for the specific indexing shown in the table.

Beam	[001], [116] [114]	[116]	[114]	[114]
Diffracting vector	$(2\bar{2}0)\mathbf{g}$	$(15\bar{1})\mathbf{g}$	$(31\bar{1})\mathbf{g}$	$(13\bar{1})\mathbf{g}$
Shift vector:				
1/4[011]	V	I	V	I
1/4[0$\bar{1}$1]	V	V	I	V
1/4[101]	V	V	I	I
1/4[$\bar{1}$01]	V	I	V	V
1/4[110]	I	I	I	V
1/4[$\bar{1}$10]	I	V	V	I
1/2[100]	I	V	V	V

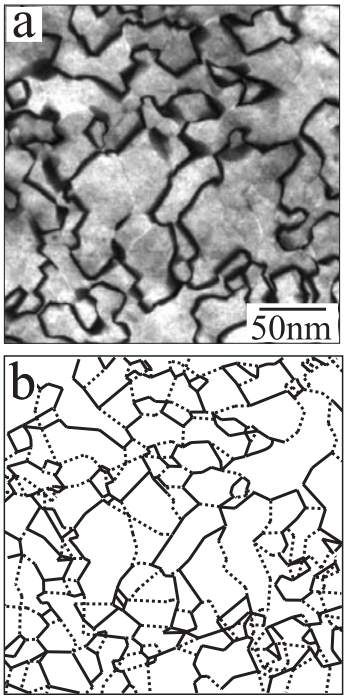

Fig. 5. For a 25 nm thick film grown at 250 °C, a) TEM dark field image near the [001] direction using the 220-type reflection that shows all of the out-of-plane APBs and b) a schematic image showing all the APBs with the out-of-plane type as full lines and the in-plane types as dashed lines.

Figure 5 shows dark field TEM images of APBs with an out-of-plane shift and corresponding schematics showing the position of all the APBs for regions in a 25 nm thick film grown at 250 °C. A significant number of the APBs, those shown dashed in the schematics, are not visible in the image taken with the 220-type reflection. When all of the APBs are taken into account the actual domain size is about 0.6 of the apparent size observed when using the 220 reflection. Presented in Table 2 are the proportions of boundary length for each specific shift in the 25 nm thick film. These proportions have been determined by analysing over 530 APBs within an area of 350×350 nm. There were very few 1/2[100] shifts, 0.9% and the vast majority were the 1/4⟨110⟩ shifts. The proportions of each of the out-of-plane shifts were similar ranging from 13 to 15.5% and the in-plane shifts were also present in relatively equal proportions of 21 to 22%. The proportion of in-plane shifts was thus greater than the out-of-plane shifts.

Table 2. Proportion of boundary length in a 25 nm thick film for all possible shift vectors.

Shift vector		Proportion of shift present
Out-of-plane shifts	1/4[011]	14.6%
	1/4[0$\bar{1}$1]	13.0%
	1/4[101]	15.5%
	1/4[$\bar{1}$01]	12.5%
In-plane shifts	1/4[110]	22.1%
	1/4[$\bar{1}$10]	21.4%
	1/2[100]	0.9%

3.4 Relationship between anti-phase shift and boundary plane

A significant proportion of the APBs with in-plane shifts 1/4[110] and 1/4[1$\bar{1}$0] were found to have boundary planes close to (110) and (1$\bar{1}$0) respectively. This means the boundary planes for these APBs tended to be perpendicular to the shift and vertical through the film.

A correlation between the out-of-plane shifts and their boundary plane was also observed which followed from the directionality and projected widths. The boundary plane tended to lie in the vicinity of the (100) or (010) that was 45° to the shift of the APB. Note that the boundary planes were spread to either side of these planes with preference to the {130}. Superimposed on this orientation was a tendency for the boundary plane to be inclined by 2 to 13° towards the shift. The only low index crystallographic planes in the range of directions and inclinations described for the APBs are the (100), (010) and the corresponding (310), (3$\bar{1}$0), (130) and (1$\bar{3}$0), which are all vertical through the film.

4 Discussion

In principle all seven of the expected APB shifts should be present in equal proportions. The possible shift vectors are 1/2[100] and 6 different 1/4⟨110⟩ type shifts [9]. The distribution of APB shift vectors is therefore expected to be 14% for 1/2[100] and 86% for 1/4⟨110⟩.

However, our observations show that the 1/2[100] type shift only occurs in very small proportions, $< 1\%$.

Anti-phase boundaries have also been reported in other spinel structures, both in single crystals [11–13] and in thin films [14,15]. In all of these cases, only shift vectors of 1/4⟨110⟩ were reported. However, in a study by Hesse and Bethge of the defect structure in $MgTiO_2$ films grown by solid state reactions, it was found that the 1/2[100]

shift is present, but seventeen times less than the 1/4⟨110⟩ shifts [16]. The fact that shift vectors of 1/2[100] are hardly observed could mean that these APBs anneal out much faster than the APBs with a 1/4⟨110⟩ shift vector, which would be the case if the former have a higher surface energy than the latter.

A schematic drawing of the APB configuration for 1/2[010] shift and (010) boundary plane is shown in Figure 6. The atomic configuration would be the same if the boundary plane were (100). In the spinel lattice, the oxygen anions surrounding a tetrahedral ions do not touch the other tetrahedra. Octahedral and tetrahedral sites only have a common corner anion. At this boundary, however, octahedral and tetrahedral sites share a common edge which is energetically unfavorable. At the boundaries with a 1/4⟨110⟩ shift the octahedral and tetrahedral sites share a common corner [11], which is energetically more favorable than sharing a common edge. This would explain the high driving force for annealing out the APBs with 1/2[100] shift. It should be noted that this kind of APB can be formed at steps on the MgO surface of a unit cell height. However, the spacing of steps is at least an order of magnitude larger than the average domain size. It is therefore not likely that steps on the substrate surface will influence the distribution and directionality of the APBs. No previous studies on the proportions of the 1/4⟨110⟩ shifts in spinel structures have been reported. There are 6 possible 1/4⟨110⟩ shifts, of which 2 are the in-plane and 4 are the out-of-plane shifts. The expected ratio of in-pane to out-of-plane shifts would thus be 1:2. However, the proportion of in-plane shifts is larger than expected, with a ratio of 0.8:1 for a 25 nm thick film. This could be related to the observed differences in the relationship between the shift vector and boundary plane for both kinds of shifts and the effect on the relative energies of the boundaries. Other studies on spinel structures have reported several relationships between the shift vectors and the boundary planes. In single crystals of $MgAl_2O_4$, the boundary plane is either (100) at 45° to the shift [12], or {110} perpendicular to the shift [13]. Single crystals of lithium ferrite also have {110} type boundary planes perpendicular to the shift [11]. In thin films of nickel ferrite the boundary planes are also {110} type perpendicular to the shift vector [14], whereas in lithium and cobalt ferrite films the boundary planes are either {110} perpendicular to the shift or {310} making an angle of 42° to the shift [15].

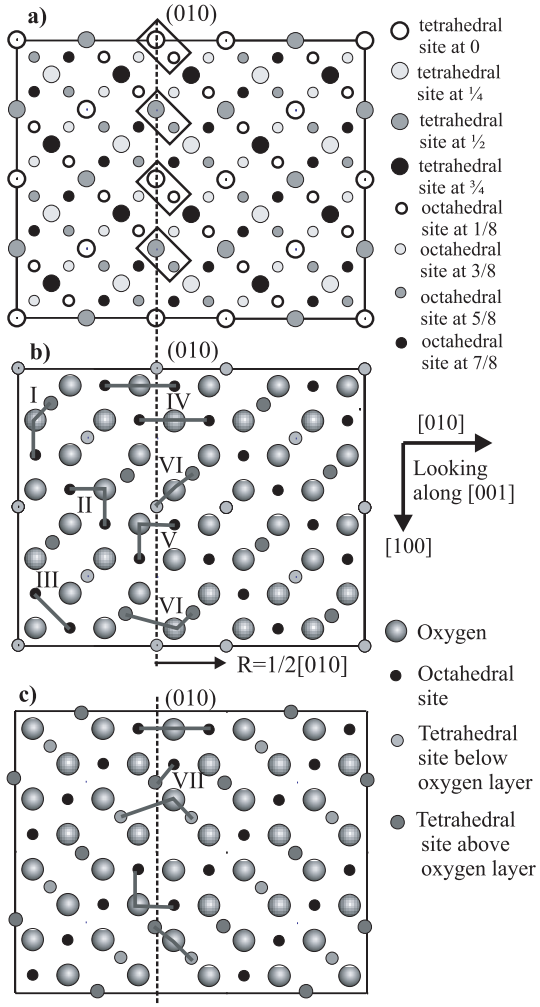

Fig. 6. Schematic drawing of a boundary with a 1/2[010] shift and (010) boundary plane. The three dimensional projection of the iron sublattice (the oxygen ions are omitted) is shown in a), where octahedral and tetrahedral sites share a common edge. b) shows the first oxygen layer with octahedral sites and the tetrahedral sites directly above and below this plane and c) shows the second layer. The third and fourth layers (not shown) are similar to the first and second layers. Examples of magnetic super-exchange interactions across the boundary are indicated as grey lines and their numbers are explained in the text.

Several arguments for the relationship between the shift and the boundary plane have been given. The lowest energy will be achieved when the introduction of the fault does not change the stoichiometry of the crystal [11]. When a shift does not lie in the boundary plane, a stoichiometric amount of material has to be either removed or inserted to form the APB. If a non-stoichiometric amount of material is inserted, the boundary is called non-conservative and will posses a higher energy [17]. When the 1/4⟨110⟩ shift lies perpendicular to the boundary plane the crystal does remain stoichiometric [11]. The lowest energy will then be achieved when the number of nearest neighbors is least changed and the distances between nearest neighbors are least altered with respect to the bulk. Van der Biest and Thomas [11] have shown that this is the case when the shift is perpendicular to the boundary plane.

This is also what we observed for many of the in-plane shifts 1/4[110] and 1/4[1$\bar{1}$0]. However, for the out-of-plane shifts, the boundary plane is not perpendicular to the shift vector. In contrast, the boundary planes are close to {100} or {310} at 45° and 42° respectively to the shift. The former family of planes was also observed in $MgAl_2O_4$ single crystals [12] and the latter was also observed for cobalt ferrite thin films [15]. The energy of these configurations is higher than for a {101} boundary plane due to smaller

distances between nearest neighbors. On the other hand, the area of the {100} and {310} boundary planes is less than for a {101} type plane which makes an angle of 45° to the foil.

The total energy of an APB will depend on its area through the film and on its crystallographic orientation. The minimization of energy seems to be an important factor, as we observed a strong domain growth at relatively low temperatures of 125 °C to 350 °C [10]. Also, the curvature of the APBs is strongly reduced upon annealing. As explained above, we would expect all shifts (and possibly also all boundary planes) to occur initially and APBs with the highest energy to anneal out the fastest. There are two observations that support this view. First, the APBs with 1/2[100] shift vector seem to anneal out much faster. Second, the boundaries with an in-plane shift and a boundary plane perpendicular to both the shift vector and the foil (and thus with minimum surface energy and area) are present in larger proportions. There indeed seems to be an anisotropy in APB energy with crystallographic planes, as observed by the increase in directionality shown by the rose diagrams in Figure 4.

Compared to other studies of spinels, the most notable difference in the APB morphology in our epitaxial Fe_3O_4 films is that the boundary planes do not lie on well defined crystallographic planes. The APBs in our study are formed due to impingement of neighboring domains and they are able to migrate via a diffusive process at relatively low temperatures. The cobalt and lithium ferrite thin films [14,15] were grown by chemical vapour deposition at high temperature (1600 °C). Consequently, at these much higher temperatures the diffusivities are much larger, enabling the APBs to migrate to proper crystallographic planes. The thermal history indeed seems to have an influence on the boundary configuration, as in $MgAl_2O_4$ single crystals, grown using a large temperature gradient, the boundary plane was not always a crystallographic plane [12]. This was interpreted as APBs lying on arbitrary planes that change their configuration so that their energy can be reduced via cation diffusion, causing the APB to have a folded configuration.

4.1 Magnetic exchange interactions at the anti-phase boundaries

The configuration of the APB is important to understand because it will influence the magnetic coupling across the APB and this can effect the physical properties of the epitaxial Fe_3O_4 films. For instance, magnetic domain walls can be pinned at the APB [6,18]. An anti-ferromagnetic coupling will have a strong influence on the magnetisation [6] and on the magneto-resistance properties [3].

Before we discuss the interactions across the boundaries, a brief review of the literature on exchange interactions in spinels is appropriate. The exchange interactions to consider in the bulk are: super-exchange between octahedral (iron)-oxygen-tetrahedral (iron), which is anti-ferromag-netic (AF) [19,20], super-exchange between octahedral-oxygen-octahedral (90°) and double exchange between octahedral iron ions, which both result in a ferromagnetic coupling (FM) between the octahedral ions [21,22]. These three exchange interactions have been indicated in Figure 6b as grey lines labelled I, II and III respectively. The interaction between tetrahedral sites can be ignored, because of the large distance between these sites [19]. The anti-ferromagnetic exchange interaction is the strongest one and is responsible for the ferrimagnetic coupling in Fe_3O_4.

Table 3. Magnetic exchange interactions across anti-phase boundaries in epitaxial Fe_3O_4 films on MgO, listed according to their relative strength.

Exchange interaction	type and angle	Strength and sign	Presence
oct-ox-oct	super, 180°	AF, strong	at APB
tet-ox-tet	super, ∼140°	AF, strong	at APB
oct-ox-tet	super, ∼120°	AF, strong	bulk and APB
oct-ox-oct	super, 90°	FM, weak	bulk and APB
tet-ox-tet	super, ∼70°	AF, weak	at APB
oct-oct	direct	FM, weak	bulk and APB
tet-tet	direct	AF, weak	at APB
oct-tet	direct	FM, weak	at APB

Across the boundary, there can be new octahedral-oxygen-octahedral interactions (180°, AF and strong, labelled IV), additional octahedral-oxygen-octahedral interactions (90°, FM and weak plus additional double exchange interactions between the octahedral iron ions, both labelled V), new tetrahedral-oxygen-tetrahedral interactions (AF and strong, labelled VI), new octahedral-tetrahedral interactions (FM and weak, labelled VII), additional octahedral-oxygen-tetrahedral interactions (AF and strong, labelled VIII), direct exchange interactions between tetrahedral sites (AF and weak, labelled IX), tetrahedral-oxygen-tetrahedral 70° (AF and weak, labelled X). All these interactions, their relative strength and presence have been summarised in Table 3. These interactions are all competing across the boundary and not all of them can be minimised simultaneously, leading to competition. The competition mainly results from the anti-ferromagnetic coupling between octahedral-oxygen-octahedral interactions and between octahedral-oxygen-tetrahedral interactions. We will explain this by examining the structure and magnetic coupling for a 1/4[110] shift with (110) boundary plane (i.e. the shift is perpendicular to the boundary plane, as has also been observed experimentally). Figure 7 shows a schematic drawing of the configuration of a 1/4[110] shift with a (110) boundary plane. In order to represent all the nearest neighbour interactions, we have drawn an oxygen-octahedral plane with the tetrahedral sites below and above this plane. This has been done for all four monolayers in the unit cell. Examples of super-exchange interactions across the boundary are indicated as grey lines. In the first monolayer (Fig. 7a) there are new octahedral-oxygen-tetrahedral interactions between an octahedral iron ion in the boundary plane and tetrahedral iron ions on both sites of this

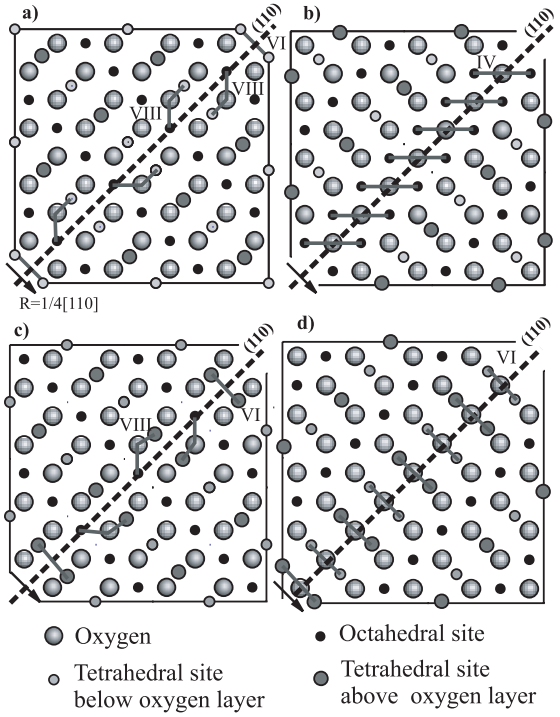

Fig. 7. Schematic drawing of a boundary with a 1/4[110] shift and (110) boundary plane. a) shows the first oxygen layer with octahedral sites and the tetrahedral sites directly above and below this plane and b), c) and d) show the second, third and fourth layer respectively. Examples of magnetic superexchange interactions across the boundary are indicated as grey lines.

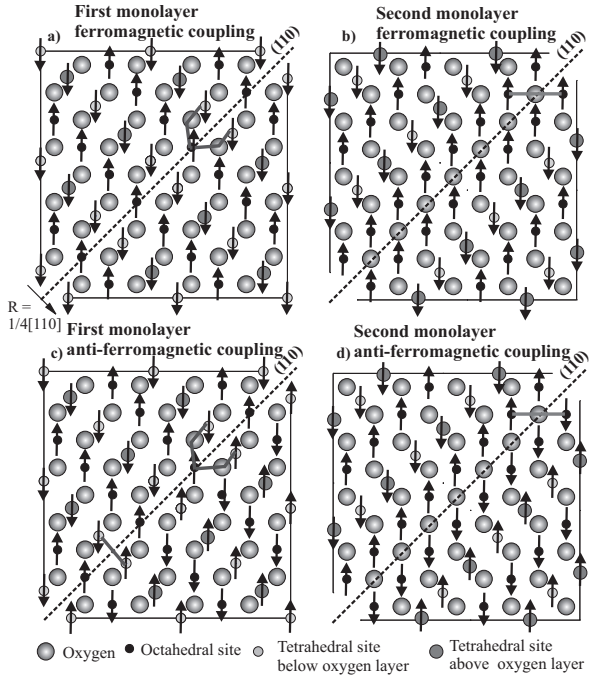

Fig. 8. Magnetic configurations for a boundary with a 1/4[110] shift and (110) boundary plane. This figure shows the magnetic moments for both a ferromagnetic alignment in between the two domains in a) and b) and an anti-ferromagnetic alignment in c) and d).

plane. This is a strong anti-ferromagnetic interaction. However, the coupling between the octahedral iron can not be anti-ferromagnetic to both of the tetrahedral ions at the same time when the two domains have an overall anti-ferromagnetic alignment. This is illustrated in Figure 8, where the magnetic configuration is drawn for the first two monolayers of this type of boundary. In Figures 8a and b the first two monolayers are drawn with an overall ferromagnetic alignment between the domains. In Figures 8c and d the same monolayers are drawn with an overall anti-ferromagnetic alignment between the domains. When the overall alignment is ferromagnetic, the coupling of the octahedral ion at the boundary can be anti-ferromagnetic with both of the tetrahedral ions on either side. But a ferromagnetic alignment leads to a problem in the second monolayer, where the octahedral-oxygen-octahedral superexchange interaction dictates an anti-ferromagnetic coupling between those ions. The number of octahedral-oxygen-tetrahedral interactions that can not be minimised simultaneously for an anti-ferromagnetic alignment between the domains is equal to the number of octahedral-oxygen-octahedral interactions that can not be minimised when the alignment between the domains is ferromagnetic. These superexchange interactions are both strong, and the octahedral-oxygen-octahedral interactions are probably slightly stronger due to the larger angle of 180°. From these considerations one could deduce that an anti-ferromagnetic alignment is slightly more favourable. However, in case of anti-ferromagnetic alignment between the domains there are also octahedral-octahedral interactions that can not be minimised, as this interaction favours a ferromagnetic alignment (this interaction is illustrated by a grey line in Fig. 8c). Therefore, both configurations are probably very similar in energy and the resulting alignment will depend on interactions with other neighbouring domains as well.

A similar analysis has been performed for the 1/2[010] shift with a (010) boundary plane using Figure 6. Most super-exchange interactions can be minimised when the magnetic alignment between the domains is anti-ferromagnetic.

All four monolayer with the tetrahedral sites above and below the planes for a 1/4[011] shift with a (010) boundary plane is shown in Figures 9a–d. Applying the same criteria as above, it is concluded that a ferromagnetic coupling between the domains has a lower energy than an anti-ferromagnetic coupling.

As observed experimentally, the boundary planes can also be close to {310}. All four monolayers with the tetrahedral sites above and below the monolayers for a 1/4[101] shift with a (130) boundary plane are shown in Figures 10a–d. In this case, the anti-ferromagnetic coupling between the domains has the lowest energy.

The fact that the shift vector is not parallel to the boundary plane, but either perpendicular or at an angle close to 45°, leads to an increase in competition between octahedral-oxygen-octahedral and octahedral-oxygen-tetrahedral interactions. In contrast to results from previous research [6,7], this more often leads to a

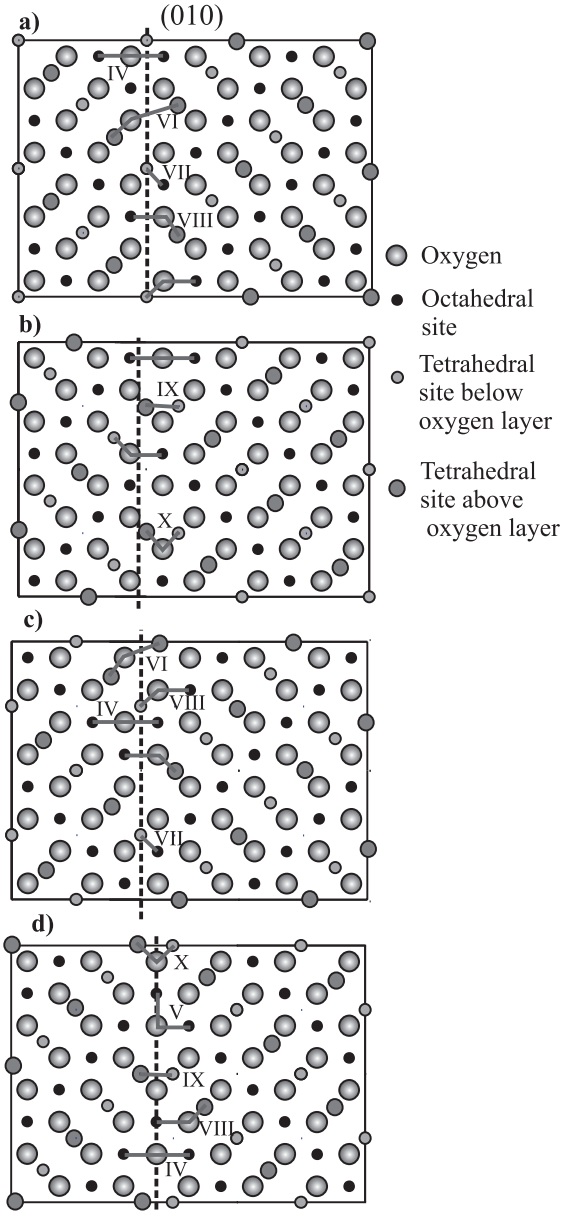

Fig. 9. Schematic drawing of a boundary with a 1/4[011] shift and (010) boundary plane. a) shows the first oxygen layer with octahedral sites and the tetrahedral sites directly above and below this plane and b), c) and d) show the second, third and fourth layer respectively. Examples of magnetic superexchange interactions across the boundary are indicated as grey lines.

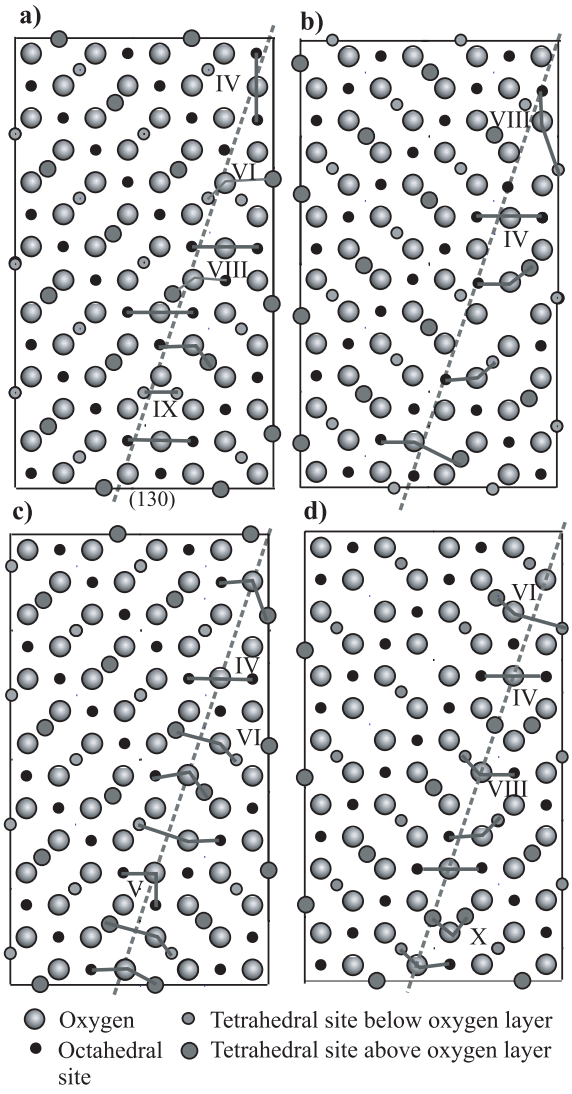

Fig. 10. Schematic drawing of a boundary with a 1/4[101] shift and (130) boundary plane. a) Shows the first oxygen layer with octahedral sites and the tetrahedral sites directly above and below this plane and b), c) and d) show the second, third and fourth layer respectively. Examples of magnetic superexchange interactions across the boundary are indicated as grey lines.

ferromagnetic instead of an anti-ferromagnetic configuration between two domains. Also, the number of anti-ferromagnetic exchange interactions at the APB itself is less than previously assumed.

5 Conclusions

We have grown epitaxial Fe_3O_4 films on MgO and studied the configuration of anti-phase boundaries occurring in these films. The APBs occur as growth defects and the possible shift vectors are 1/2[100] and 1/4⟨110⟩. We studied the distribution of shift vectors, the relation between the shift vector and the boundary plane and the directionality of the APBs. At some of these APBs an anti-ferromagnetic coupling is present and the APBs have a strong influence on resistivity, magnetism and magnetoresistance properties of these films. The 1/2[100] shift was hardly observed, less than 1% was of this type. This probably means the APBs with 1/2[100] shift vectors anneal out quickly because they posses a higher APB energy than APBs with 1/4⟨110⟩ shift. APBs with an in-plane shift vector, 1/4[110] and 1/4[1$\bar{1}$0] have their boundary planes perpendicular to the shift vector, (110) and (1$\bar{1}$0) respectively. In this case, the magnetic alignment between the

two domains can be either ferromagnetic or anti-ferromagnetic and 45% of the boundaries are of this type. The four possible out-of-plane shift vectors were also expected have the boundary planes perpendicular to the shift. This was however not the case, but the boundary plane was either close to {100} or {310} which was related to a reduction in APB energy by minimizing the total boundary area. The magnetic coupling across these boundaries is ferromagnetic when the boundary plane is {100} and anti-ferromagnetic when the boundary plane is {310}. The resulting magnetic configuration is therefore not always anti-ferromagnetic.

This work was funded by the Netherlands Organisation for Scientific Research (NWO). The authors thank H.J. Bruinenberg for technical assistance and J. Wheeler and R.C. Pond for scientific discussions. The authors further thank M. Bestmann for assistance with the image analysis.

References

1. J.M.D. Coey, A.E. Berkowitz, Ll. Balcells, F.F. Putris, F.T. Parker, Appl. Phys. Lett. **72**, 734 (1998)
2. M. Ziese, H.J. Blyte, J. Phys.: Condens. Matter **12**, 13 (2000)
3. W. Eerenstein, T.T.M. Palstra, S.S. Saxena, T. Hibma, Phys. Rev. Lett. **88**, 247204 (2002)
4. R.J.M. van de Veerdonk, M.A.M. Gijs, P.A.A. van der Heijden, R.M. Wolf, W.J.M. de Jonge, Mat. Res. Soc. Symp. Proc. **401**, 455 (1996)
5. W. Eerenstein, T.T.M. Palstra, T. Hibma, S. Celotto, Phys. Rev. B **66**, 201101(R) (2002)
6. D.T. Margulies, F.T. Parker, M.L. Rudee, F.E. Spada, J.N. Chapman, P.R. Aitchison, A.E. Berkowitz Phys. Rev. Lett. **79**, 5162 (1997)
7. F.C. Voogt, T.T.M. Palstra, L. Niesen, O.C. Rogojanu, M.A. James, T. Hibma, Phys. Rev. B **57**, R8107 (1998)
8. F.C. Voogt, T. Fujii, P.J.M. Smulders, L. Niesen, M.A. James, T. Hibma, Phys. Rev. B **60**, 11193 (1999)
9. T. Hibma, F.C. Voogt, L. Niesen, P.A.A. van der Heijden, W.J.M. de Jonge, J.J.T.M. Donkers, P.J. van der Zaag, J. Appl. Phys. **85**, 5291 (1999)
10. W. Eerenstein, S. Celotto, T.T.M. Palstra, T. Hibma, Phys. Rev. B. **68**, 014428 (2003)
11. O. van der Biest, G. Thomas, Phys. Stat. Solidi (a) **24**, 65 (1974)
12. M.H. Lewis, Phil. Mag. **14**, 1003 (1966)
13. H. Tabata, H. Okuda, E. Ishii, Jpn J. Appl. Phys. **12**, 7 (1973)
14. A.G. Fitzgerald, R. Engin, Thin Solid Films **20**, 317 (1974)
15. A.G. Fitzgerald, T.G. May, Thin Solid Films **35**, 201 (1976)
16. D. Hesse, H. Bethge, J. Crystal Growth **65**, 69 (1983)
17. A. Putnis, J.D.C. McConnell, *Principles of Mineral Behaviour* (Blackwell Scientific, Oxford 1980), pp. 122–123
18. A.J. Lapworth, J.P. Jakubovics, G.S. Baker, J. Phys. Colloq. France **32**, C1-259 Suppl. n° 2-3 (1974)
19. P.G. Bercoff, H.R. Bertorello, J. Magn. Magn. Mater. **169**, 314 (1997)
20. C.M. Srivastava, G. Srinivasa, N.G. Nanadikar, Phys. Rev. B **19**, 499 (1979)
21. P.A. Cox, *Transition Metal Oxides* (Oxford University Press, Oxford 1995), pp. 221–223
22. J.D. Goodenough, *Magnetism and the Chemical Bond* (Wiley, New York 1963), pp. 165–185